Article

Discovery Medicine 2026; 38(209): 2013–2029
https://doi.org/10.24976/Discov.Med.202638209.156

Indoxyl Sulfate Induces Ferroptosis via the AhR/ACSL4 Axis to Mediate Uremic Cardiomyopathy

Dianhua Zhou[1,2,†], Zhubin Lun[2,†], Wenwei Feng[2], Xiaohan Ye[2], Jianfeng Ye[2,*], Jianfang Luo[1,*]

[1]Department of Cardiology, Guangdong Provincial People's Hospital, Guangdong Academy of Medical Sciences, Southern Medical University, 510080 Guangzhou, Guangdong, China
[2]Department of Cardiology, Dongguan Traditional Chinese Medicine Hospital, The Ninth Clinical Medical College of Guangzhou University of Chinese Medicine, 523005 Dongguan, Guangdong, China
*Correspondence: yipjf@hotmail.com (Jianfeng Ye); jianfangluo@sina.com (Jianfang Luo)
[†]These authors contributed equally.
Submitted: 13 April 2026 Revised: 22 May 2026 Accepted: 29 May 2026 Published: 20 June 2026

Background: Uremic cardiomyopathy is a leading cause of cardiovascular death in chronic kidney disease (CKD), yet the cell death mechanisms linking uremic toxins to myocardial injury remain unclear. Indoxyl sulfate (IS), a protein-bound uremic toxin and endogenous aryl hydrocarbon receptor (AhR) ligand, has been implicated in cardiotoxicity; however, whether it induces cardiomyocyte ferroptosis through a defined signaling pathway remains to be investigated. This study aimed to determine whether IS induces cardiomyocyte ferroptosis via an AhR/Acyl-CoA synthetase long-chain family member 4 (ACSL4) signaling axis and to evaluate its contribution to uremic cardiomyopathy.

Methods: A 5/6 nephrectomy CKD mouse model was used to characterize myocardial ferroptosis in the uremic setting. H9c2 cardiomyocytes were treated with IS, with or without the AhR antagonist CH-223191, ferrostatin-1, or ACSL4-targeting siRNA, to dissect the upstream signaling mechanism. An IS injection model combined with AAV9-mediated cardiac-targeted ACSL4 knockdown was employed to evaluate ACSL4's role *in vivo*.

Results: CKD mice exhibited elevated serum IS alongside myocardial ferroptosis signatures and cardiac remodeling (all $p < 0.001$). IS promoted AhR nuclear translocation and ACSL4 upregulation in cardiomyocytes ($p < 0.001$), both of which were attenuated by CH-223191 ($p < 0.001$). Bioinformatic analysis identified multiple xenobiotic response element motifs in the ACSL4 promoter. ACSL4 silencing or ferrostatin-1 attenuated IS-induced lipid peroxidation and rescued cell viability *in vitro* (all $p < 0.001$). Cardiac-targeted ACSL4 knockdown alleviated IS-induced hypertrophy, fibrosis, and myocardial ferroptosis *in vivo* without altering systemic IS levels (all $p < 0.001$).

Conclusion: Using complementary CKD and direct IS exposure models, we demonstrate that IS exposure is sufficient to induce cardiomyocyte ferroptosis in association with AhR-dependent upregulation of ACSL4, and that cardiac-targeted ACSL4 knockdown attenuates IS-induced cardiac injury *in vivo*. The AhR/ACSL4/ferroptosis axis represents a potential pathogenic mechanism in uremic cardiomyopathy and a candidate therapeutic target.

Keywords: indoxyl sulfate; ferroptosis; aryl hydrocarbon receptor; ACSL4; uremic cardiomyopathy; chronic kidney disease

Introduction

Chronic kidney disease (CKD) affects roughly 10–13% of the global adult population, and cardiovascular disease is the leading cause of death in this population [1]. Among patients receiving hemodialysis, cardiovascular disease accounts for nearly 50% of deaths [2]. Uremic cardiomyopathy, characterized by left ventricular hypertrophy, diffuse interstitial myocardial fibrosis, and diastolic dysfunction, is a common cardiovascular complication of CKD that becomes progressively more pronounced as kidney function declines [3,4]. Despite considerable technical and scientific advances in renal replacement therapy, cardiovascular morbidity and mortality remain disproportionately high, underscoring the need to elucidate the molecular mechanisms underlying myocardial injury in the uraemic milieu [5]. Among the potential mediators, protein-bound uremic toxins, particularly indoxyl sulfate and p-cresyl sulfate, have emerged as important CKD-specific, non-traditional mediators of direct cardiac remodeling and toxicity beyond conventional hemodynamic risk factors [6]. Indoxyl sulfate (IS), a tryptophan-derived protein-bound uremic toxin generated through gut microbial metabolism, accumulates progressively as glomerular filtration declines [7]. Elevated IS levels have been associated with all-cause mortality and have been identified as an independent predictor of adverse cardiovascular outcomes in several patients with CKD [8]. Experimental studies further show that

IS promotes cardiomyocyte hypertrophy, oxidative stress, and pro-fibrotic signaling [6,9]. However, the precise cell death mechanism through which IS exerts its cardiotoxic effects remains incompletely defined.

Ferroptosis is a recently recognized form of regulated cell death characterized by iron-dependent phospholipid peroxidation [10]. Unlike apoptosis and necroptosis, ferroptosis is morphologically distinguished by mitochondrial shrinkage, increased membrane density, and cristae reduction, while it is biochemically characterized by lipid peroxide accumulation, typically accompanied by glutathione depletion and glutathione Peroxidase 4 (GPX4) inactivation [10,11]. Ferroptosis has been implicated in diverse cardiovascular pathologies, including myocardial ischemia-reperfusion injury, doxorubicin-induced cardiomyopathy, and diabetic cardiomyopathy [12–14]. Recent research has reported ferroptotic features in CKD- and uremia-associated organ injury [15]. However, whether ferroptosis serves as a mechanistic link between uremic toxin exposure and myocardial injury remains insufficiently explored and has not yet been systematically reviewed [16].

Acyl-CoA synthetase long-chain family member 4 (ACSL4) has emerged as a key determinant of ferroptosis sensitivity [17]. ACSL4 promotes the incorporation of polyunsaturated fatty acids (PUFAs), particularly arachidonic acid, into membrane phospholipids, thereby generating lipid substrates susceptible to iron-dependent peroxidation [18]. Pharmacological inhibition of ACSL4, together with genetic ablation or knockdown in selected models, confers robust protection against ferroptosis in multiple organ systems [19,20]. In the heart, increased ACSL4 expression has been linked to ferroptotic myocardial injury [21]. However, whether and how uremic stress regulates ACSL4 expression in cardiomyocytes remains unclear.

The aryl hydrocarbon receptor (AhR) is a ligand-activated transcription factor that, upon ligand binding, translocates to the nucleus, heterodimerizes with AhR nuclear translocator (ARNT), and binds xenobiotic response elements (XREs) in the promoters of target genes to regulate transcription [22]. IS is a bona fide endogenous agonist of AhR, and AhR activation has been implicated in IS-induced vascular inflammation, endothelial dysfunction, and oxidative stress [23]. Notably, because IS is an established endogenous AhR ligand [24] and ACSL4 is transcriptionally regulated at the promoter level [25], putative XRE-like motifs within the ACSL4 promoter could potentially mediate AhR-dependent transcriptional upregulation in response to IS, although direct experimental validation of such binding has not been established.

Despite these converging lines of evidence, whether IS induces cardiomyocyte ferroptosis through an AhR/ACSL4 signaling axis has not been investigated. We hypothesized that IS activates AhR signaling, leading to upregulation of ACSL4 and subsequent ferroptosis-mediated cardiac injury. To test this hypothesis, we employed a 5/6 nephrectomy CKD mouse model to establish clinical relevance, an IS injection model combined with AAV9-mediated cardiac-targeted ACSL4 knockdown for *in vivo* functional validation, and *in vitro* mechanistic studies in H9c2 cardiomyocytes. Our results identified the AhR/ACSL4/ferroptosis axis as a critical pathogenic mechanism in IS-induced cardiac injury.

Materials and Methods

Animals and Ethical Approval

Male C57BL/6 mice (8–10 weeks old; body weight 22–25 g) were obtained from Beijing Vital River Laboratory Animal Technology Co., Ltd. (Beijing, China). Animals were housed under specific pathogen-free conditions (12 h light/dark cycle, 22–24 °C, 40–60% humidity) with ad libitum access to standard chow and water. All animal procedures were approved by the Institutional Animal Care and Use Committee of Guangzhou University of Chinese Medicine (Approval No. 20250104008), and performed in accordance with the National Institutes of Health Guide for the Care and Use of Laboratory Animals. A total of 32 male C57BL/6 mice were used in this study. Two mice died following 5/6 nephrectomy surgery and were replaced. Data are reported for the final cohort of 30 mice, comprising 12 mice for the 5/6 nephrectomy CKD model experiment (sham, n = 6; 5/6 Nx, n = 6) and 18 mice for the IS injection model with AAV9-mediated cardiac ACSL4 knockdown (Control, n = 6; IS + AAV9 empty vector, n = 6; IS + AAV9-shACSL4, n = 6).

Study Design, Randomization, and Blinding

Mice were randomly assigned to experimental groups using a computer-generated random number sequence. Group allocation was concealed from investigators performing treatment and outcome assessment by using coded animal identifiers. Histological and immunohistochemical quantifications were performed on coded slides by an investigator blinded to group allocation, with group identities decoded only after completion of data quantification.

Pre-specified exclusion criteria included death before the designated experimental endpoint, unsuccessful establishment of the CKD model, and technical failure during tissue processing or assay. Of the 8 mice subjected to 5/6 nephrectomy, 2 died during the postoperative period and were replaced. No animals were excluded from the final analysis after model establishment. In all *in vivo* analyses, each data point represents an individual animal (biological replicate). In all *in vitro* experiments, each data point represents an independent experiment.

CKD Model by 5/6 Nephrectomy

A 5/6 nephrectomy (Nx) CKD model was established in C57BL/6 mice, with sham-operated animals serving as controls (Sham vs 5/6 Nx) [26,27]. Briefly, mice were anes-

thetized with pentobarbital sodium (50 mg/kg, i.p.; Sigma-Aldrich, St. Louis, MO, USA, Cat# P3761) and placed on a heating pad to maintain body temperature. A two-step 5/6 Nx procedure, including two-thirds of the left kidney, was ablated by ligating two of three extrarenal branches of the left renal artery, and the intact right kidney was removed one week later. Sham mice underwent identical surgical exposure without renal mass reduction. Postoperative analgesia was provided using buprenorphine (0.1 mg/kg, s.c.; Cayman Chemical Company, Ann Arbor, MI, USA, Cat# 14025) every 12 h for 3 days. Animals were monitored daily and sacrificed (overdose of pentobarbital sodium, 150 mg/kg, i.p., followed by cervical dislocation) at 8 weeks after model induction for sample collection.

IS Injection Model and in Vivo Cardiac ACSL4 Knockdown

To investigate the role of ACSL4 in IS-induced cardiac injury, an indoxyl sulfate (IS) intraperitoneal injection model was used. Mice were randomly allocated to three groups (n = 6 per group): Control (saline + AAV9 empty vector), IS + AAV9 (IS + AAV9 empty vector), and IS + AAV9-shACSL4 (IS + ACSL4 knockdown).

AAV9 vectors carrying either short hairpin RNA against ACSL4 (AAV9-cTnT-shACSL4; AAV9-shACSL4) or an empty cassette (AAV9-cTnT-Scramble; AAV9 empty vector) driven by the cardiomyocyte-specific cardiac troponin T (cTnT) promoter were produced by Hanbio Biotechnology Co., Ltd. (Shanghai, China). The cardiomyocyte-specific cTnT promoter ensures the selective expression of the shACSL4 cassette in cardiomyocytes. Because transgene expression is regulated by promoter activity rather than by AAV9 capsid biodistribution, ACSL4 knockdown is expected to be confined to cardiomyocytes, despite the potential distribution of AAV9 genomes to other tissues. Knockdown efficiency in cardiac tissue was verified at the protein level by Western blotting (Fig. 6A). The experimental timeline was defined relative to the day of AAV9 administration, which was designated as Week 0 (Day 0). AAV9 was administered via tail vein injection at Week 0 to allow sufficient cardiac expression prior to toxin challenge. Mice received either AAV9-shACSL4 or AAV9 empty vector at a dose of 1×10^{11} viral genomes (vg)/mouse in 100 µL sterile PBS. Beginning at Week 3, mice were injected intraperitoneally with IS daily for 4 weeks (from week 3 to week 7). IS (Sigma-Aldrich, St. Louis, MO, USA, Cat# I3875) was dissolved in sterile saline and administered at 100 mg/kg/day in a final volume of 200 µL. Control mice received volume-matched saline injections. At the end of Week 7 (24 h after the final IS injection), blood and cardiac tissues were collected for biochemical, histological, and molecular analyses. Mice were euthanized by overdose of pentobarbital sodium (150 mg/kg, i.p.) and sacrificed by cervical dislocation.

Serum Biochemistry and ELISA

Blood was collected via retro-orbital puncture under anesthesia and centrifuged at 3000 g for 15 min at 4 °C to obtain serum. Serum creatinine and blood urea nitrogen (BUN) were measured with commercial kits (Nanjing Jiancheng Bioengineering Institute, Nanjing, China, Cat# C011-2-1 and C013-2-1, respectively) to confirm renal dysfunction in the CKD model. Total serum indoxyl sulfate was quantified using an ELISA kit (FineTest, Wuhan, China, Cat# EM1922) following the manufacturer's instructions. All samples were assayed in duplicate against a standard curve generated in parallel. According to the manufacturer's validation data, the assay has a detection sensitivity of 0.938 ng/mL and a detection range of 1.563–100 ng/mL. ELISA was selected as a widely used and accessible method for the relative comparison of serum IS levels between experimental groups in rodent studies. Serum B-type natriuretic peptide (BNP) was measured by an ELISA kit (Jiyinmei Biotech, Wuhan, China, Cat#JYM0759Mo).

Cardiac Morphometry (HW/TL and HW/BW)

Following euthanasia (as described above; overdose of pentobarbital sodium at 150 mg/kg, i.p., with cervical dislocation as secondary confirmation), hearts were rapidly excised, rinsed in cold PBS, blotted dry, and weighed. Tibia length (TL) was measured using digital calipers. Heart weight was normalized to tibia length (HW/TL) and body weight (HW/BW) to assess cardiac hypertrophy.

Masson's Trichrome and WGA Staining

Hearts were fixed in 4% paraformaldehyde (MedChemExpress, Monmouth Junction, NJ, USA, Cat# HY-Y0333) for 36 h, processed, and embedded in paraffin. Paraffin-embedded sections (4 µm) were stained with Masson's trichrome (Servicebio, Wuhan, China, Cat# G1006) to assess myocardial fibrosis. Stained sections were imaged under a Nikon Eclipse Ci-L upright light microscope equipped with a Nikon DS-Fi3 digital camera (Nikon Corporation, Tokyo, Japan) at 200× and 400× magnification. Fibrotic area was quantified as the percentage of collagen-stained area relative to total myocardial area using ImageJ software (version 1.53, National Institutes of Health, Bethesda, MD, USA) from 5 random fields per section and 3 sections per heart.

For cardiomyocyte hypertrophy assessment, deparaffinized sections were incubated with wheat germ agglutinin (WGA) conjugate to Alexa Fluor 488 (Thermo Fisher Scientific, Waltham, MA, USA, Cat# W11261) at a concentration of 5 µg/mL for 30 min at room temperature to outline cell membranes, and nuclei were counterstained with DAPI (Beyotime, Shanghai, China, Cat# C1006). Fluorescent images were acquired using a Nikon Eclipse Ti2 inverted fluorescence microscope (Nikon Corporation, Tokyo, Japan) equipped with appropriate filter sets for Alexa Fluor 488 (excitation 488 nm, emission 525 nm) and DAPI (excitation

358 nm, emission 461 nm) at 400× magnification. Cardiomyocyte cross-sectional area (CSA) was quantified by measuring ≥100 cardiomyocytes per heart from 3 sections using ImageJ software (version 1.53, National Institutes of Health, Bethesda, MD, USA).

4-HNE Immunohistochemistry

Lipid peroxidation was evaluated by immunostaining for 4-hydroxynonenal (4-HNE). After antigen retrieval in PBS (pH 7.4) and blocking with 3% BSA, sections were incubated with anti-4-HNE primary antibody (Servicebio, Wuhan, China, Cat# GB150073-100; 1:200 dilution) overnight at 4 °C, followed by HRP-conjugated secondary antibody for IHC (Servicebio, Wuhan, China, Cat# GB23301). Signals were developed using a DAB kit (TIANGEN, Beijing, China, Cat# PA110) for IHC. Stained sections were imaged under a Nikon Eclipse Ci-L upright light microscope equipped with a Nikon DS-Fi3 digital camera (Nikon Corporation, Tokyo, Japan) at 200× and 400× magnification. Quantification was performed as integrated optical density (IOD)/area (IHC) using Image-Pro Plus software (version 6.0, Media Cybernetics, Rockville, MD, USA) from 3 random fields per section.

Prussian Blue Staining

Myocardial iron deposition was assessed by Prussian blue staining using a commercial kit (Solarbio, Beijing, China, Cat# G1422) according to the manufacturer's protocol. The iron-positive area was quantified as a percentage of the total myocardial area using ImageJ from 5 random fields per section.

Cell Culture and Treatments

Rat cardiomyoblast H9c2 cells were obtained from the Cell Bank of the Chinese Academy of Sciences (Shanghai, China) and cultured in high-glucose DMEM (Gibco, Thermo Fisher Scientific, Grand Island, NY, USA, Cat# 11965092) supplemented with 10% fetal bovine serum (FBS; Gibco, Thermo Fisher Scientific, Grand Island, NY, USA, Cat# 10099141) and 1% penicillin/streptomycin (Gibco, Thermo Fisher Scientific, Grand Island, NY, USA, Cat# 15140122) at 37 °C in 5% CO_2. The cell line was authenticated by Short Tandem Repeat (STR) profiling and tested negative for mycoplasma contamination.

For upstream signaling experiments (Fig. 2), H9c2 cells were treated with IS at 0.5 mM for 24 h [9,28], a concentration and exposure duration that has been widely used in previous *in vitro* studies of IS-induced cardiomyocyte injury [9,28], with or without the AhR antagonist CH-223191 (MedChemExpress, Monmouth Junction, NJ, USA, Cat# HY-12684; 10 µM; pre-treatment for 1 h). Groups included Control, IS, and IS + CH-223191.

For downstream functional experiments (Fig. 4), groups consist of Control, IS, IS + ferrostatin-1 (Fer-1; MedChemExpress, Monmouth Junction, NJ, USA, Cat# HY-100579), IS + si-NC, and IS + si-ACSL4. Fer-1 is a lipophilic radical-trapping antioxidant that selectively inhibits ferroptosis by scavenging lipid peroxyl radicals and thereby suppressing phospholipid peroxidation, and it is widely used as a pharmacological tool to confirm the involvement of ferroptosis in cell death [29]. Fer-1 was added at 2 µM 1 h prior to IS exposure and maintained throughout the treatment.

Table 1. Primer sequences.

Name	Sequences (5′-3′)
RAT-ACSL4-F	TCGATCCCAGGAGATTGACC
RAT-ACSL4-R	GCGTGACAGAGCGATATGGA
RAT-AhR-F	TCCCGTGTCTTTCAGCTGTC
RAT-AhR-R	TATCAGGAAGAGGCTGGGCT
RAT-GAPDH-F	ATGATTCTACCCACGGCAAG
RAT-GAPDH-R	CTGGAAGATGGTGATGGGTT

ACSL4, Acyl-CoA synthetase long-chain family member 4; AhR, aryl hydrocarbon receptor; GAPDH, Glyceraldehyde-3-phosphate dehydrogenase.

siRNA Transfection

siRNA targeting ACSL4 (si-ACSL4) and negative control siRNA (si-NC) were purchased from GenePharma (Shanghai, China). Cells were transfected using Lipofectamine 3000 (Thermo Fisher Scientific, Waltham, MA, USA, Cat# L3000015) according to the manufacturer's protocol. Typically, cells at 50–70% confluency were transfected with siRNA at 50 nM for 24 h before IS stimulation. Knockdown efficiency was validated by Western blotting for ACSL4.

Quantitative Real-Time PCR (qPCR)

Total RNA was isolated using TRIzol reagent (TIANGEN, Beijing, China, Cat# DP424). cDNA was synthesized with a PrimeScript RT Reagent Kit (Takara Bio Inc., Shiga, Japan, Cat# RR037A). qPCR was performed using SYBR Green SuperReal PreMix Plus (TIANGEN, Beijing, China, Cat# FP205) on a LightCycler96 (Roche, Basel, Switzerland) system. Relative expression was calculated using the $2^{-\Delta\Delta Ct}$ method, normalized to GAPDH. Primers for ACSL4 and AhR are present in Table 1.

Nuclear and Cytosolic Fractionation

To assess AhR nuclear translocation, nuclear and cytosolic proteins were isolated using a Nuclear and Cytoplasmic Protein Extraction Kit (Beyotime, Cat# P0028). AhR abundance in nuclear fractions was analyzed by Western blotting. Histone H3 served as a nuclear marker.

Western Blotting

Protein was extracted from heart tissues or H9c2 cells using RIPA lysis buffer (Beyotime, Shanghai, China, Cat# P0013J) containing protease and phosphatase in-

hibitors (Beyotime, Shanghai, China, Cat# ST506). Protein concentrations were determined using a BCA kit (Beyotime, Shanghai, China, Cat# P0012S). Equal amounts of protein (30 μg) were separated by SDS-PAGE and subsequently transferred onto PVDF membranes (Millipore, Billerica, MA, USA, Cat# IPVH00010). Membranes were blocked with 5% non-fat milk in TBST for 1 h and incubated overnight at 4 °C with primary antibodies against ACSL4 (HUABIO, Hangzhou, China, Cat# HA601112, 1:1000), GPX4 (HUABIO, Hangzhou, China, Cat# ER1803-15, 1:1000), AhR (HUABIO, Hangzhou, China, Cat# ET1703-11, 1:1000), and loading controls (GAPDH, Proteintech, Rosemont, IL, USA, Cat# 60004-1-Ig, 1:100; H3, HUABIO, Hangzhou, China, Cat# ET1701-64, 1:200,000). After incubation with HRP-conjugated secondary antibodies (ZSGB-Bio, Beijing, China, Cat# ZB-2305/ZB-2301, 1:2000), signals were detected using enhanced chemiluminescence (ECL) substrate (Millipore, Billerica, MA, USA, Cat# WBKLS0500) and quantified by densitometry with ImageJ.

Lipid Peroxidation Assay in Cells (C11-BODIPY) and Cell Viability (CCK-8)

Lipid peroxidation in H9c2 cells was measured using the C11-BODIPY 581/591 probe (Thermo Fisher Scientific, Waltham, MA, USA, Cat# D3861) followed by flow cytometry. Cells were incubated with C11-BODIPY (2 μM) for 30 min at 37 °C, washed with PBS, and analyzed on a BD FACSCanto II flow cytometer (BD Biosciences, San Jose, CA, USA) with appropriate settings. Lipid peroxidation was reported as the percentage of oxidized C11-BODIPY-positive cells.

Cell viability was assessed using a CCK-8 kit (Dojindo Laboratories, Kumamoto, Japan, Cat# CK04) according to the manufacturer's instructions. Briefly, 10 μL CCK-8 reagent was added to each well and incubated for 1.5 h. Absorbance was measured at 450 nm using a microplate reader (BECKMAN Coulter, Inc., Brea, CA, USA, Cat# PK7300).

Measurement of Myocardial MDA and GSH/GSSG

Myocardial lipid peroxidation products and redox status were quantified using commercial assay kits for malondialdehyde (MDA; Beyotime, Shanghai, China, Cat# S0131S) and GSH/GSSG ratio (Beyotime, Shanghai, China, Cat# S0053) following the manufacturer's protocols. Heart tissues were homogenized in cold PBS, centrifuged at 12,000 g for 10 min at 4 °C, and supernatants were used for measurements. Results were normalized to protein content.

Bioinformatic Prediction of AhR Binding Sites in the ACSL4 Regulatory Region

To assess whether AhR may directly regulate ACSL4 at the transcriptional level, the rat ACSL4 regulatory region (2003 bp upstream of the transcription start site [TSS] through the first intron; RefSeq NM_053623.1, rn7 assembly) was retrieved from the UCSC Genome Browser (https://genome.ucsc.edu/). The sequence was scanned for putative aryl hydrocarbon receptor/AhR nuclear translocator (AhR::ARNT) binding motifs using the JASPAR position weight matrix MA0006.1 (https://jaspar.elixir.no/) with a relative score threshold of ≥85%. In parallel, a sequence pattern search was performed to identify canonical xenobiotic response element (XRE) core motifs (5′-GCGTG-3′ and its reverse complement 5′-CACGC-3′) within the same region.

Statistical Analysis

Statistical analyses were performed using GraphPad Prism (9.5.1; GraphPad Software, San Diego, CA, USA). Data are presented as mean ± SEM. Normality of data distribution was assessed using the Shapiro-Wilk test, and all datasets satisfied the normality assumption ($p > 0.05$). Homogeneity of variance was confirmed using Levene's test prior to parametric analysis. For comparisons between two groups, an unpaired two-tailed Student's *t*-test was used. For three or more groups, one-way ANOVA followed by Tukey's post hoc test was applied. A p value < 0.05 was considered statistically significant. The sample size of n = 6 per group was determined based on previous studies employing similar CKD and IS injection mouse models, which demonstrated sufficient statistical power to detect biologically meaningful differences in cardiac remodeling and ferroptosis-related indices. For all analyses, n refers to the number of individual animals for *in vivo* experiments or independent experiments for *in vitro* studies, and each plotted data point represents one such replicate.

Results

CKD Induces Systemic IS Accumulation and Cardiac Ferroptosis, Accompanied by Uremic Cardiomyopathy Phenotypes

To establish the clinical relevance and recapitulate the CKD-associated cardiac phenotype, a murine CKD model was generated via 5/6 nephrectomy (5/6 Nx), with samples collected 8 weeks after surgery. As expected, CKD mice displayed marked renal dysfunction, as indicated by elevated serum creatinine (Scr) and blood urea nitrogen (BUN) compared with sham-operated controls (Fig. 1A; $p < 0.001$). Consistent with impaired renal clearance, CKD mice exhibited significant accumulation of the uremic toxin indoxyl sulfate (IS) in serum (Fig. 1B; $p < 0.001$). Then, phenotypes associated with uremic cardiomyopathy were assessed. Serum BNP was significantly increased in CKD mice (Fig. 1C; $p < 0.001$), accompanied by increased cardiac hypertrophy indices HW/TL and HW/BW (Fig. 1D; $p < 0.001$). Histologically, CKD hearts showed increased interstitial fibrosis by Masson's trichrome staining (Fig. 1E;

$p < 0.001$) and cardiomyocyte hypertrophy by WGA staining (Fig. 1F; $p < 0.001$). Together, these data confirm that 5/6 nephrectomy induces a robust uremic cardiomyopathy phenotype with concurrent systemic IS accumulation.

Subsequently, whether ferroptosis is activated in the CKD myocardium was investigated. CKD hearts exhibited enhanced 4-HNE immunostaining (Fig. 2A; $p < 0.001$) and increased iron deposition by Prussian blue staining (Fig. 2B; $p < 0.001$), supporting activation of ferroptotic pathology *in vivo*. At the molecular level, CKD myocardium displayed increased ACSL4 and decreased GPX4 protein expression (Fig. 2C; $p < 0.001$), together with biochemical evidence of oxidative stress, including increased MDA and an altered GSH/GSSG redox state (Fig. 2D; $p < 0.001$).

IS Activates AhR Signaling and Is Associated With ACSL4 Induction in Cardiomyocytes

To interrogate the upstream mechanism by which IS regulates ACSL4, H9c2 cardiomyocytes were treated with IS in the presence or absence of the AhR antagonist CH-223191. IS significantly increased ACSL4 protein abundance, whereas this effect was markedly attenuated by CH-223191 (Fig. 3A; $p < 0.001$). In parallel, quantitative PCR demonstrated that IS increased ACSL4 mRNA, which was significantly reduced by CH-223191 (Fig. 3B; $p < 0.001$). Importantly, total AhR mRNA expression did not substantially change across treatment groups (Fig. 3C; $p > 0.05$), indicating that AhR activation, rather than increased AhR abundance, may be the key event linking IS to ACSL4 transcription. Consistent with AhR activation, nuclear fractionation showed that IS promoted AhR nuclear translocation, characterized by increased AhR in the nuclear fraction (Fig. 3D; $p < 0.001$). CH-223191 effectively blocked this nuclear accumulation, restoring nuclear AhR levels toward control levels (Fig. 3D; $p < 0.001$).

To provide *in silico* support for direct transcriptional regulation of ACSL4 by AhR, bioinformatic scanning of the rat ACSL4 regulatory region was performed using the JASPAR AhR::ARNT position weight matrix (MA0006.1). Six canonical XRE core motifs (GCGTG/CACGC) were identified, of which four were located within the promoter region (–1774, –391, –180, and –64 bp relative to the TSS), one in the 5'UTR (+45 bp), and one in the first intron (+1338 bp) (**Supplementary Fig. 1**). Notably, two XRE sites at –391 and –180 bp map to the proximal promoter, a region typically enriched for functional transcription factor binding. These findings suggest that the ACSL4 promoter harbors multiple putative AhR-responsive elements, providing *in silico* support for a possible AhR-dependent transcriptional regulation of ACSL4 upon IS stimulation. However, direct binding of AhR to these elements remains to be experimentally validated.

ACSL4 Mediates IS-Induced Lipid Peroxidation and Ferroptotic Injury in Cardiomyocytes

To test whether ACSL4 is functionally required for IS-induced ferroptosis, H9c2 cells were assigned to the following groups: Control, IS, IS + ferrostatin-1 (Fer-1), IS + si-NC, and IS + si-ACSL4. Lipid peroxidation was quantified using C11-BODIPY. IS exposure markedly increased oxidized C11-BODIPY fluorescence compared with control cells, while Fer-1 or ACSL4 knockdown substantially reduced the IS-induced lipid peroxidation signal (Fig. 4A,B; all $p < 0.001$). Consistent with ferroptotic injury, IS significantly decreased cell viability as measured by CCK-8, and this reduction was not altered by si-NC. In contrast, Fer-1 treatment or si-ACSL4 significantly rescued cell viability (Fig. 4C; $p < 0.001$). At the protein level, IS reduced GPX4 expression, whereas GPX4 levels were partially preserved in the Fer-1 or si-ACSL4 groups (Fig. 4D; $p < 0.001$). ACSL4 protein abundance increased following IS treatment, remained high in the si-NC group, and was significantly reduced in the si-ACSL4 group, confirming effective knockdown. Notably, Fer-1 did not significantly reduce ACSL4 abundance, consistent with its role downstream of lipid peroxidation (Fig. 4D; $p < 0.001$).

Cardiac-Targeted ACSL4 Knockdown Attenuates IS-Induced Cardiac Remodeling and Myocardial Ferroptosis Without Altering Systemic IS Exposure

To evaluate the functional contribution of cardiac ACSL4 to IS-induced cardiac injury *in vivo*, an IS injection model with cardiac-targeted ACSL4 knockdown was established using AAV9. IS administration markedly elevated serum IS relative to control, and AAV9-shACSL4 did not reduce serum IS levels, confirming comparable systemic toxin burden between the IS and IS + AAV9-shACSL4 groups (Fig. 5A; $p < 0.001$). IS injection significantly increased serum BNP (Fig. 5B; $p < 0.001$) and cardiac hypertrophy indices HW/TL and HW/BW (Fig. 5C; $p < 0.001$), all of which were attenuated by AAV9-shACSL4. Histological analyses further supported a protective role: IS increased myocardial fibrosis by Masson's trichrome staining (Fig. 5D; $p < 0.001$) and cardiomyocyte cross-sectional area by WGA staining (Fig. 5E; $p < 0.001$), both of which were alleviated by AAV9-shACSL4.

We then assessed ferroptosis-associated markers in the myocardium. At the molecular level, IS induced an ACSL4-high/GPX4-low protein signature, which was reversed by AAV9-shACSL4 (Fig. 6A; $p < 0.001$). IS enhanced lipid peroxidation as reflected by increased 4-HNE staining, whereas AAV9-shACSL4 reduced 4-HNE signals (Fig. 6C; $p < 0.001$). Prussian blue staining showed increased myocardial iron deposition in IS-treated mice, which was decreased by AAV9-shACSL4 (Fig. 6D; $p < 0.001$). Biochemically, IS elevated MDA levels and disrupted the GSH/GSSG redox balance, while AAV9-shACSL4 reversed these alterations (Fig. 6B; $p < 0.001$).

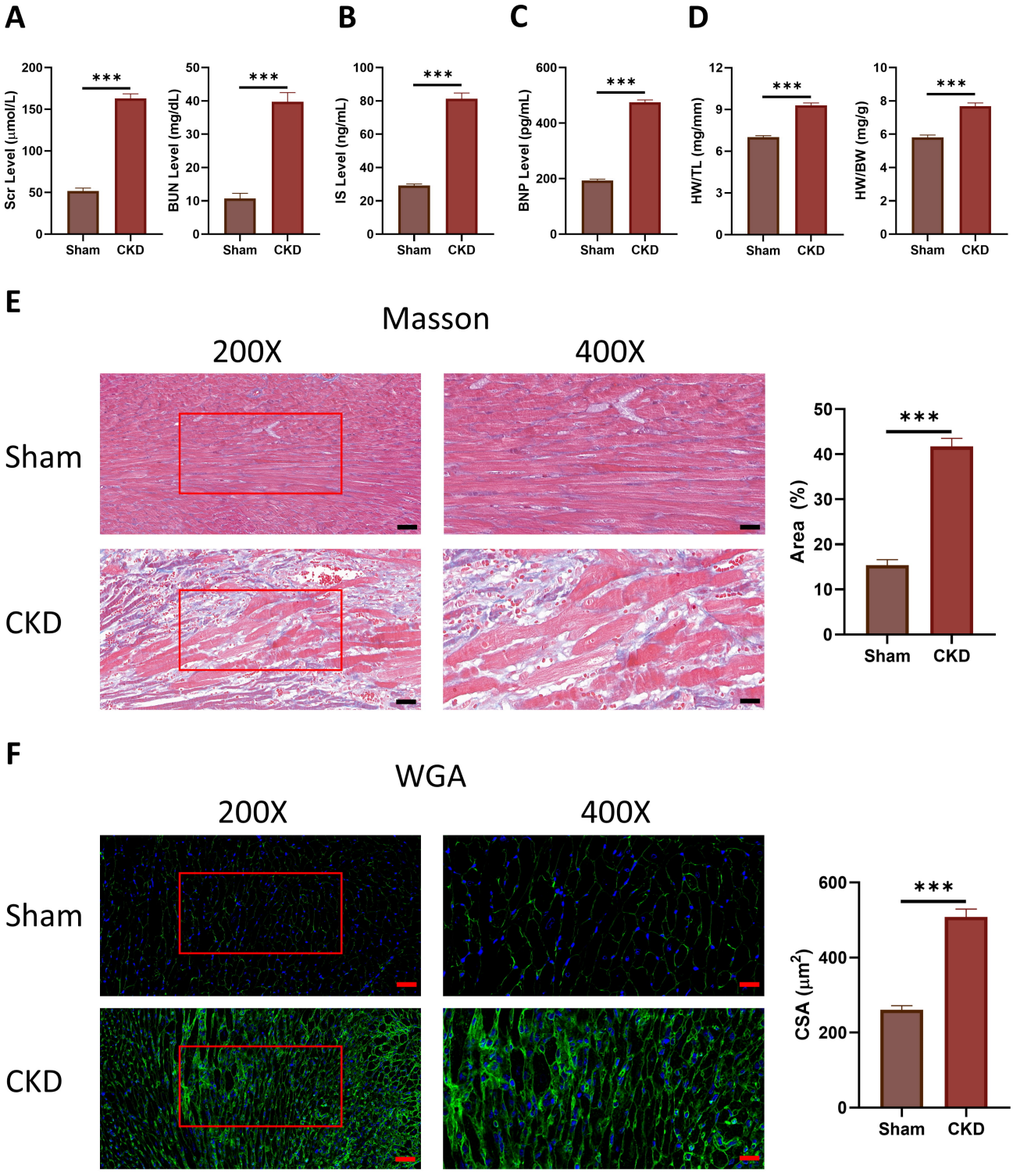

Fig. 1. CKD elevates circulating indoxyl sulfate and is associated with cardiac remodeling. (A) Serum creatinine and blood urea nitrogen (BUN) levels in sham and 5/6 nephrectomy (Nx) CKD mice. (B) Serum indoxyl sulfate (IS) levels measured by ELISA. (C) Serum B-type natriuretic peptide (BNP) levels measured by ELISA. (D) Heart weight normalized to tibia length (HW/TL) and body weight (HW/BW). (E) Representative Masson's trichrome staining of cardiac sections and quantification of fibrotic area. (F) Representative wheat germ agglutinin (WGA) staining and quantification of cardiomyocyte cross-sectional area (CSA). Data are presented as mean ± SEM. n = 6 animals per group. Statistical analysis: unpaired two-tailed Student's *t*-test (sham vs CKD). Scale bars: 100 μm for 200× and 50 μm for 400×. ***$p < 0.001$. CKD, chronic kidney disease.

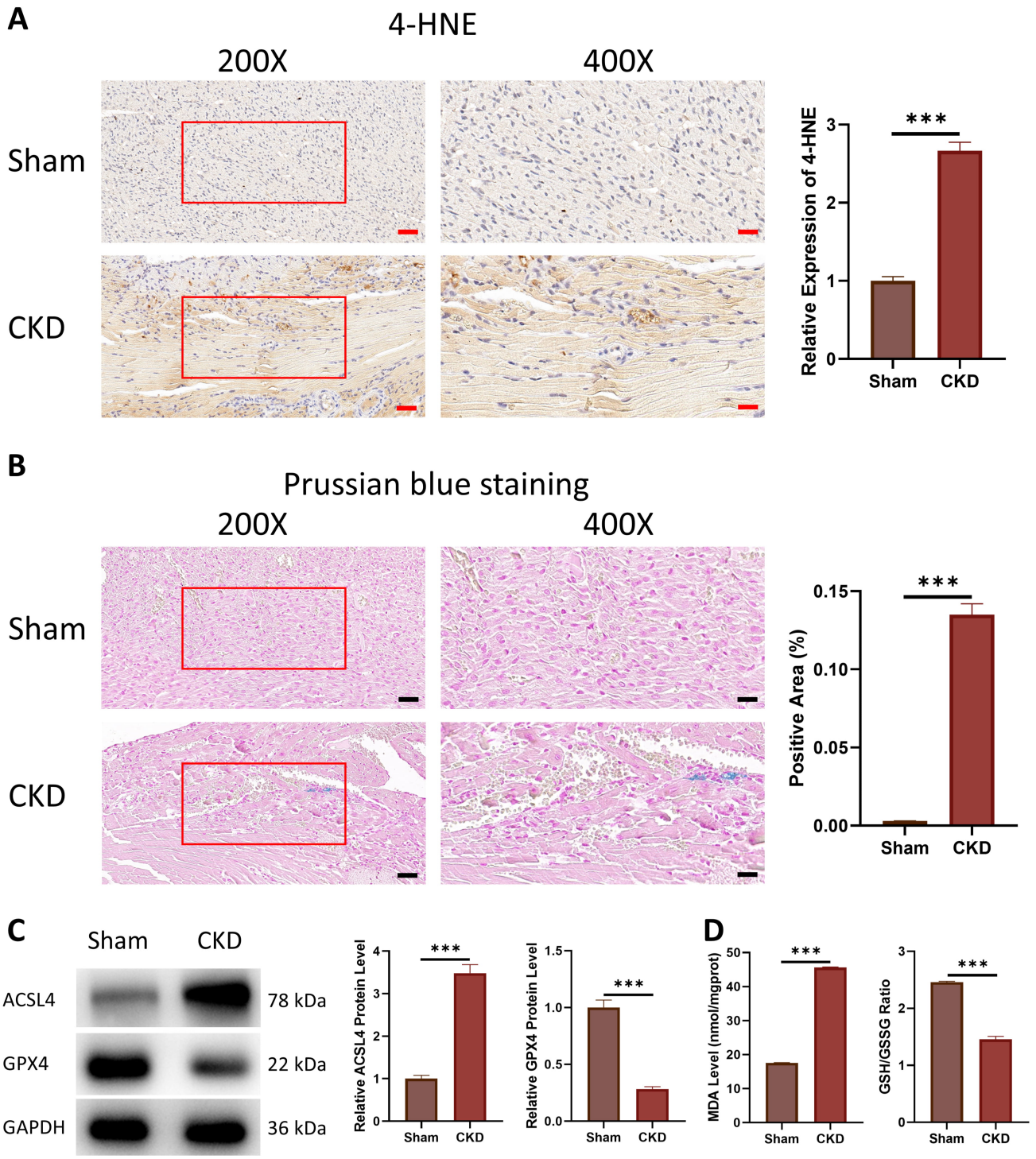

Fig. 2. CKD is associated with myocardial ferroptosis signatures. (A) Representative 4-hydroxynonenal (4-HNE) staining (IHC) and quantitative analysis. (B) Representative Prussian blue staining of myocardial iron deposition and quantification of positive area. (C) Representative immunoblots and densitometric quantification of ACSL4 and GPX4. (D) Biochemical measurements of malondialdehyde (MDA) and the GSH/GSSG ratio in myocardial tissue. Data are presented as mean ± SEM. n = 6 animals per group. Statistical analysis: unpaired two-tailed Student's *t*-test (sham vs CKD). Scale bars: 100 µm for 200× and 50 µm for 400×. ***$p < 0.001$.

Together, these findings demonstrate that cardiac ACSL4 knockdown protects against IS-induced cardiac remodeling and suppresses myocardial ferroptosis without altering systemic IS exposure.

Discussion

Uremic cardiomyopathy is a leading cause of cardiovascular morbidity and mortality in patients with CKD,

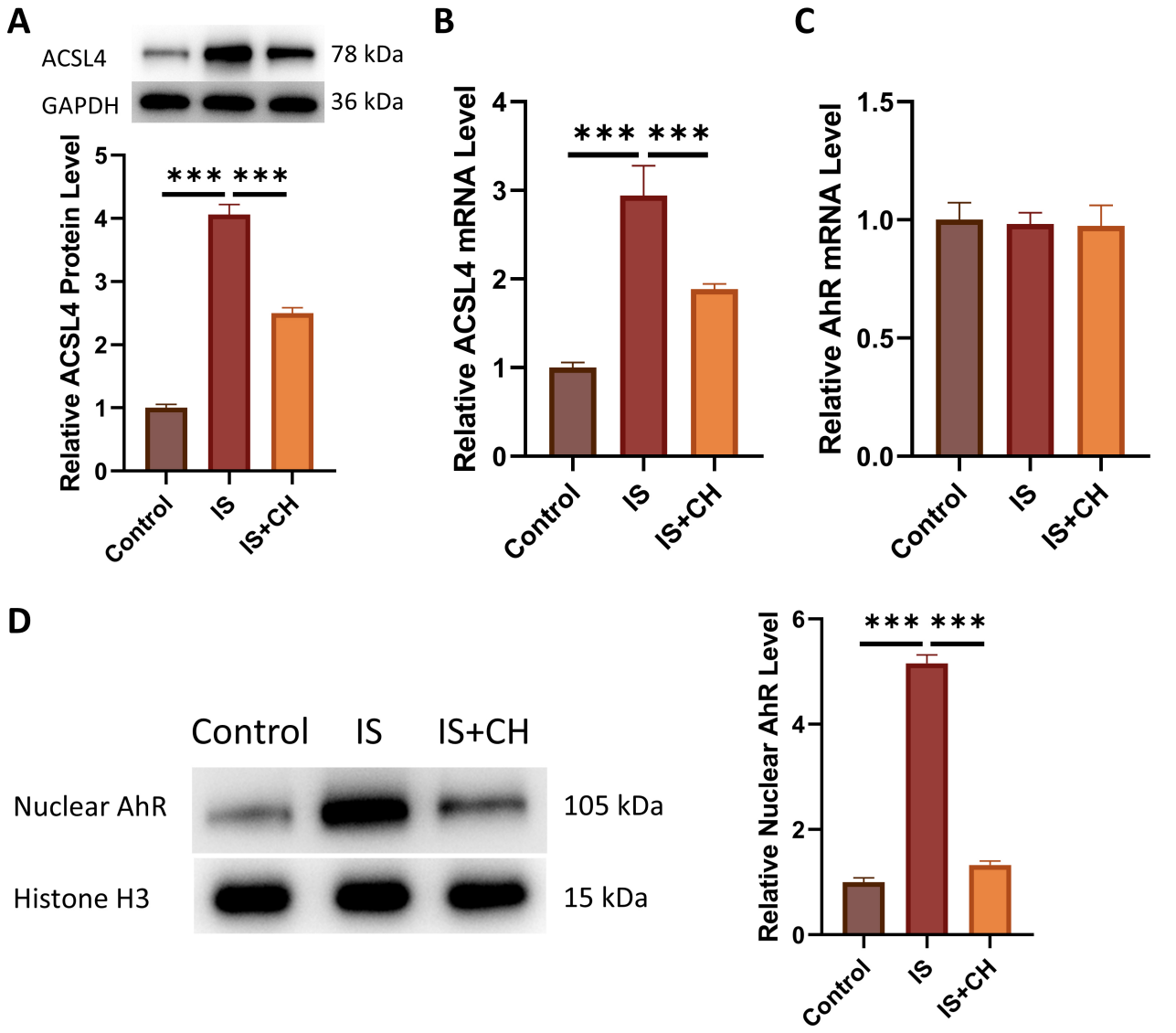

Fig. 3. Indoxyl sulfate activates AhR signaling and induces ACSL4 expression in cardiomyocytes. (A) ACSL4 protein expression measured by Western blotting and densitometry in the Control, IS, and IS + CH-223191 groups. (B) ACSL4 mRNA expression determined by qPCR. (C) AhR mRNA expression determined by qPCR. (D) AhR nuclear translocation assessed by nuclear fractionation and Western blotting; quantification shown as nuclear AhR (normalized to Histone H3). Data are presented as mean ± SEM from n = 6 independent experiments (biological replicates). Statistical analysis: one-way ANOVA with Tukey's multiple-comparisons test. ***$p <$ 0.001. AhR, aryl hydrocarbon receptor; CH, CH-223191.

yet the molecular mechanisms linking uremic toxin accumulation to myocardial injury remain incompletely understood. In the present study, we demonstrate that IS, a protein-bound uremic toxin that accumulates in CKD, induces cardiomyocyte ferroptosis via the AhR/ACSL4 signaling axis, thereby contributing to uremic cardiomyopathy. Specifically, we show that CKD mice exhibit concurrent IS accumulation and myocardial ferroptosis signatures alongside cardiac hypertrophy and fibrosis, and IS activates AhR nuclear translocation to upregulate ACSL4 in cardiomyocytes. Additionally, ACSL4 is functionally required for IS-induced lipid peroxidation and ferroptotic cell death *in vitro*, and cardiac-targeted ACSL4 knockdown alleviates IS-induced cardiac remodeling and suppresses myocardial ferroptosis *in vivo* without altering systemic IS exposure. These findings identify the AhR/ACSL4 axis as a critical mechanistic link between uremic toxin exposure and ferroptosis-mediated cardiac injury.

Our initial characterization of the 5/6 nephrectomy CKD model confirmed several features of uremic cardiomyopathy, including elevated serum BNP, increased cardiac mass indices, interstitial fibrosis, and cardiomyocyte hypertrophy. Importantly, CKD mice exhibited marked IS accumulation alongside multiple molecular and biochemical features consistent with ferroptosis in the myocardium, including enhanced 4-HNE immunostaining,

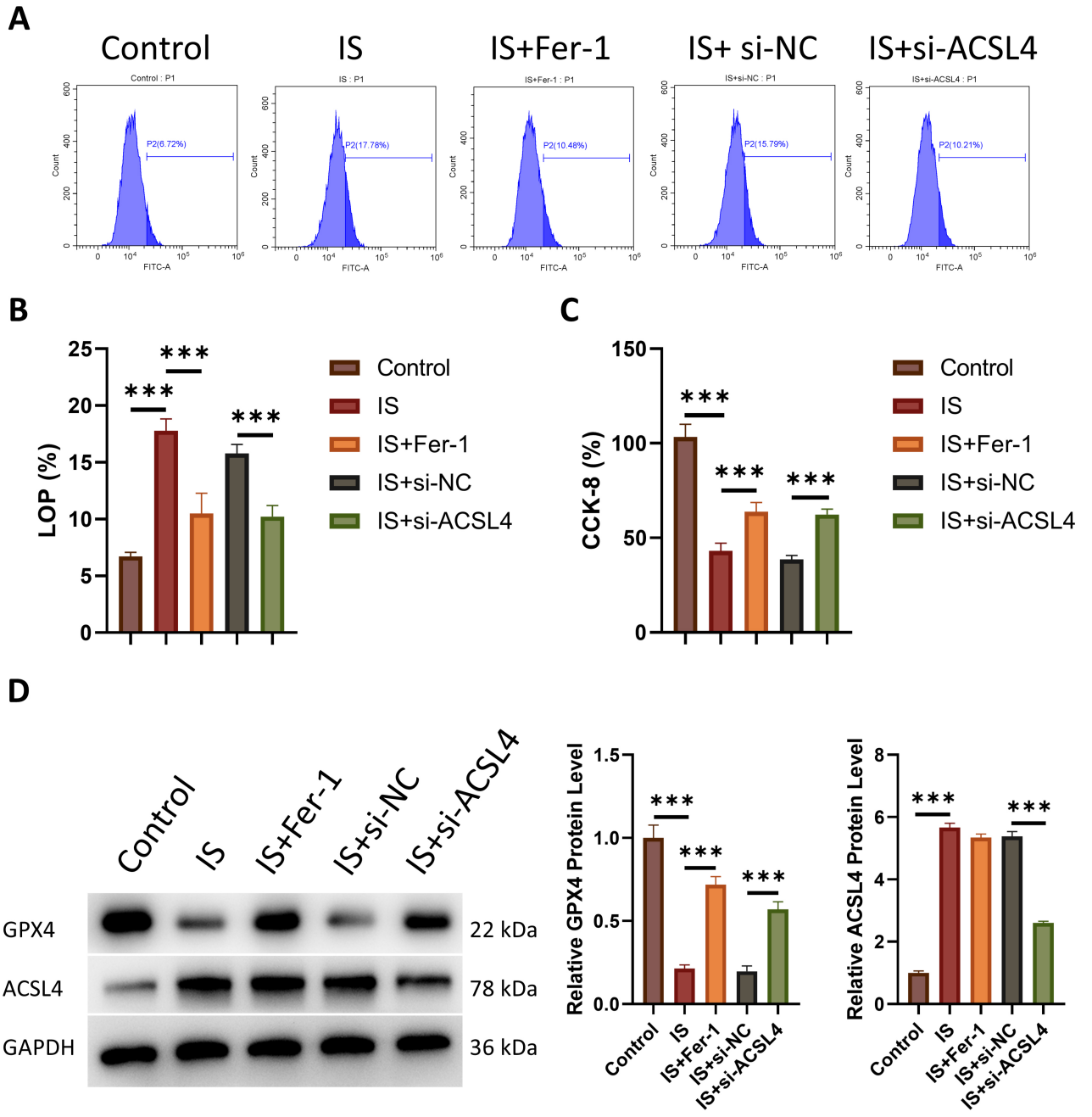

Fig. 4. ACSL4 is required for IS-induced lipid peroxidation and ferroptotic injury *in vitro*. (A) Representative flow cytometry plots of C11-BODIPY fluorescence showing lipid peroxidation in each group. (B) Quantification of lipid peroxidation based on oxidized C11-BODIPY signal (percentage of oxidized-positive cells). (C) Cell viability measured by CCK-8 assay (normalized to Control). (D) GPX4 and ACSL4 protein expression measured by Western blotting. Data are presented as mean ± SEM from n = 6 independent experiments. Statistical analysis: one-way ANOVA with Tukey's multiple-comparisons test. ***$p < 0.001$. Fer-1, ferrostatin-1; si-NC, negative-control siRNA.

Prussian blue-positive iron deposition, ACSL4 upregulation, GPX4 downregulation, elevated MDA, and a disrupted GSH/GSSG ratio. Although these observations are correlative and cannot establish causality on their own, they provide critical clinical relevance by demonstrating the co-occurrence of a ferroptotic phenotype with uremic toxin accumulation and cardiac remodeling in a well-validated CKD model. To formally test whether IS itself is sufficient to drive cardiomyocyte ferroptosis in the absence of other uremic perturbations, and thereby move beyond the correlative observations from the 5/6 Nx model, we employed a complementary direct IS injection model in non-CKD mice. In this gain-of-function paradigm, daily intraperitoneal IS administration for 4 weeks recapitulated key features of

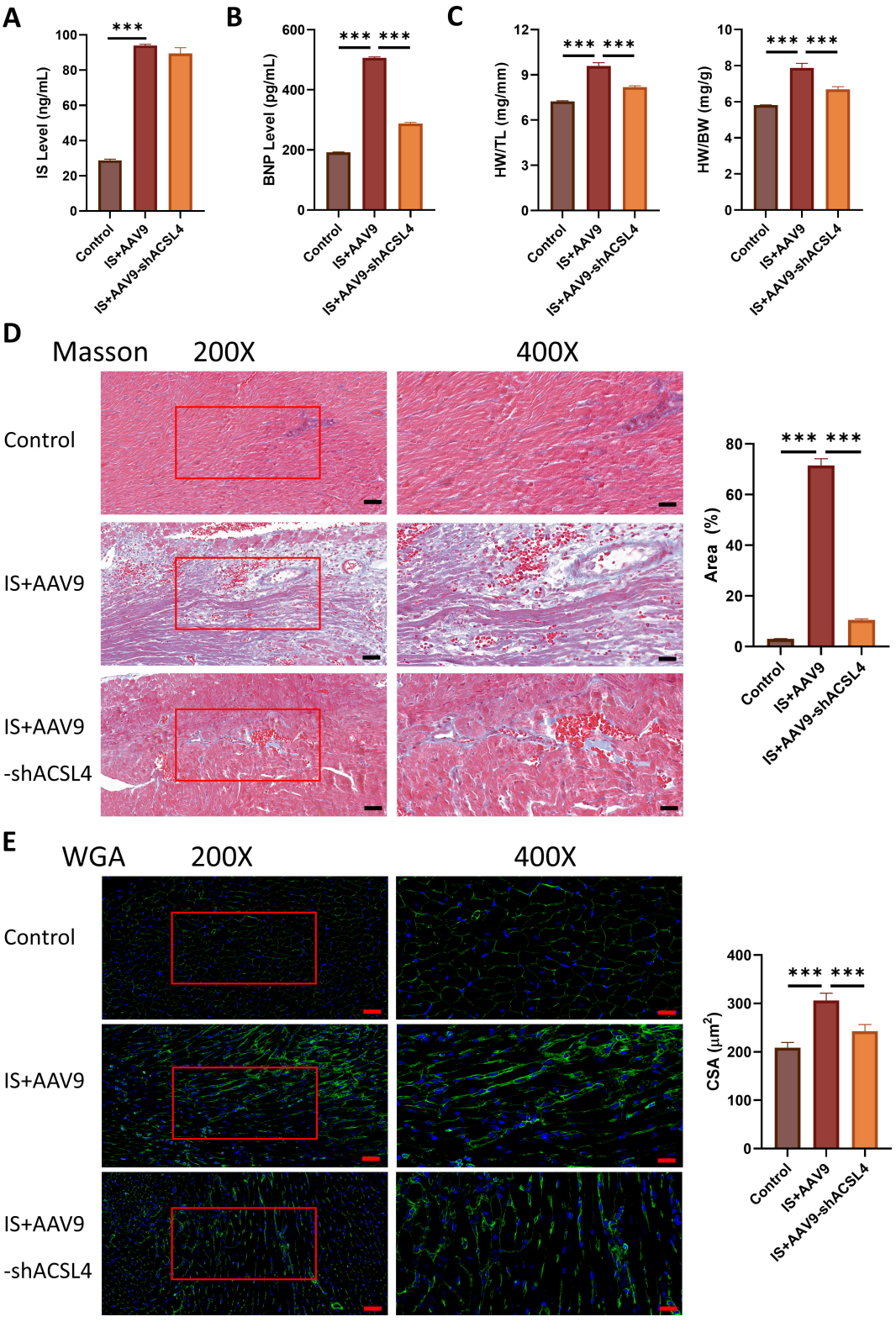

Fig. 5. Cardiac-targeted ACSL4 knockdown does not alter systemic IS levels but attenuates IS-induced cardiac remodeling *in vivo*. (A) Serum IS concentrations measured at the experimental endpoint. Groups consist of Control (saline + empty vector), IS + AAV9 (IS + empty vector), and IS + AAV9-shACSL4 (IS + ACSL4 knockdown). (B) Serum BNP levels measured by ELISA. (C) HW/TL and HW/BW indices of cardiac hypertrophy. (D) Representative Masson's trichrome staining and quantification of myocardial fibrosis. (E) Representative WGA staining and quantification of cardiomyocyte cross-sectional area (CSA). Data are presented as mean ± SEM. n = 6 animals per group. Statistical analysis: one-way ANOVA with Tukey's multiple-comparisons test. Scale bars: 100 μm for 200× and 50 μm for 400×. ***$p < 0.001$.

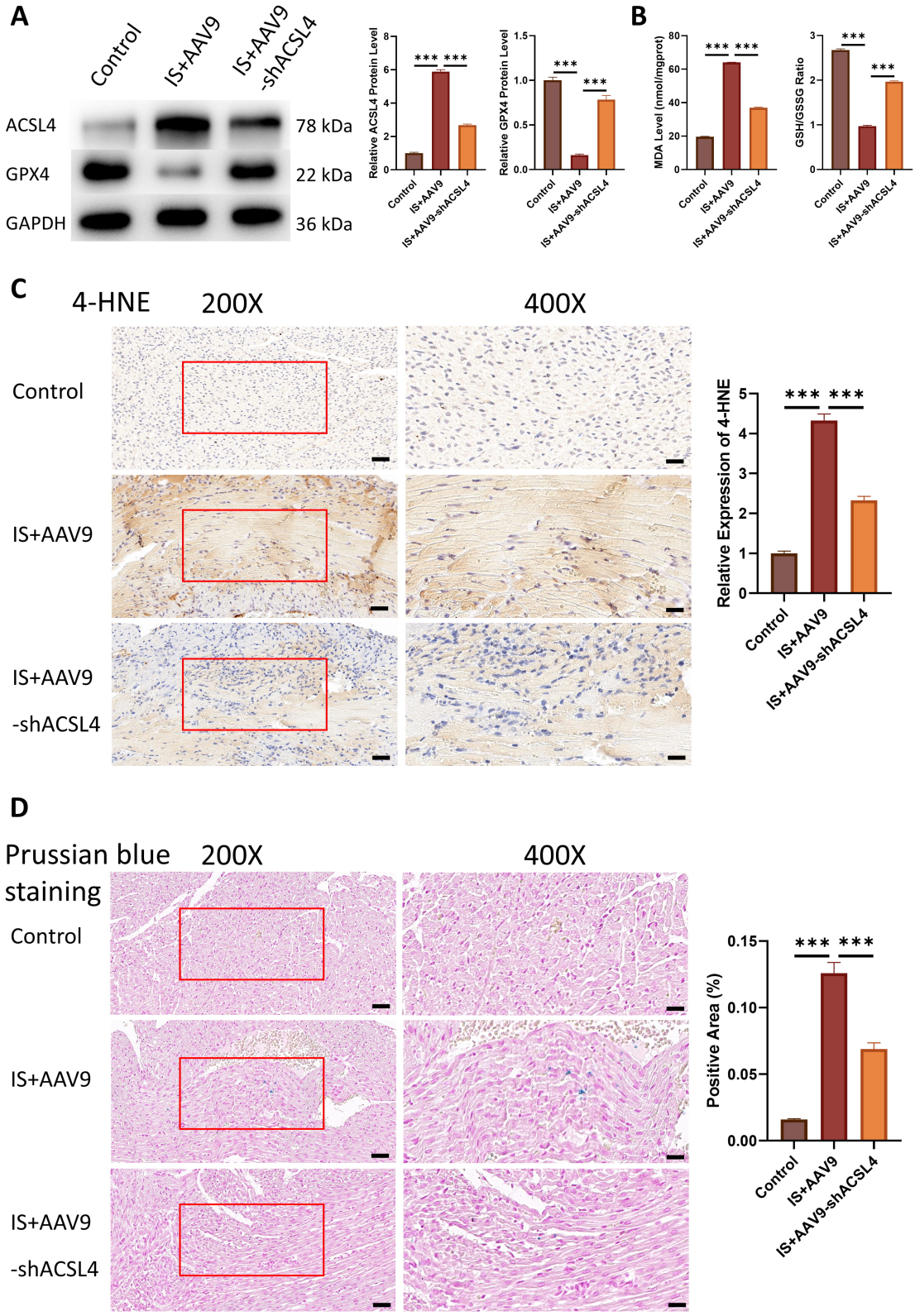

Fig. 6. Cardiac-targeted ACSL4 knockdown suppresses myocardial ferroptosis *in vivo*. (A) The protein levels of ACSL4 and GPX4 determined by Western blotting. (B) Cardiac MDA content and GSH/GSSG ratio measured by biochemical assays. (C) Representative 4-HNE staining and quantitative analysis of lipid peroxidation in cardiac tissue. (D) Representative Prussian blue staining and quantification of myocardial iron deposition. Data are presented as mean ± SEM. n = 6 animals per group. Statistical analysis: one-way ANOVA with Tukey's multiple-comparisons test. Scale bars: 100 µm for 200× and 50 µm for 400×. ***$p < 0.001$. MDA, malondialdehyde; GSH, reduced glutathione; GSSG, oxidized glutathione.

uremic cardiomyopathy, including cardiac hypertrophy, interstitial fibrosis, and myocardial ferroptosis markers, in the absence of renal dysfunction or other CKD-associated metabolic perturbations. This isolation of IS as a single experimental variable provides causal evidence that IS exposure alone is sufficient to induce cardiomyocyte ferroptosis, complementing the correlative findings from the 5/6 Nx model. Furthermore, cardiac-targeted ACSL4 knockdown by AAV9-shACSL4 attenuated IS-induced cardiac injury *in vivo* without altering systemic IS levels, establishing ACSL4 as a necessary downstream mediator and further substantiating the causal chain from IS exposure to cardiomyocyte ferroptosis. It is important to note that this cardiac-targeted ACSL4 knockdown was performed in the IS injection model rather than in the 5/6 Nx CKD model. The present experimental design nonetheless provides converging support for the proposed axis. The 5/6 Nx model demonstrates that ACSL4 upregulation and ferroptotic signatures are indeed present in the myocardium of animals with bona fide CKD, while the loss-of-function experiment in the IS injection model establishes that ACSL4 is functionally required for IS-induced myocardial ferroptosis and cardiac remodeling. Given that IS is among the principal protein-bound uremic toxins that accumulate in our 5/6 Nx model, these complementary findings suggest that ACSL4-dependent ferroptosis also contributes to myocardial injury in true CKD. However, we acknowledge that performing cardiac-targeted ACSL4 knockdown directly within the 5/6 Nx CKD model would provide the most direct evidence that ACSL4 is a pathogenic mediator of uremic cardiomyopathy, representing an important and logical next step for future investigation. The convergent evidence from these two complementary *in vivo* models, together with the *in vitro* mechanistic studies, provides a coherent causal framework, although we acknowledge that this framework does not exclude contributions from other uremic toxins to myocardial ferroptosis in the broader CKD context. It is equally important to note that the direct IS injection model, by design, does not reproduce the multifactorial uremic milieu of CKD, including renal dysfunction, hypertension, anemia, disturbed phosphate/FGF23 homeostasis, systemic inflammation, and the broader spectrum of retained uremic solutes, all of which may independently or synergistically influence myocardial ferroptosis. The cardiac phenotypes observed in the IS injection model should therefore be interpreted as the specific contribution of IS exposure, rather than as a comprehensive recapitulation of uremic cardiomyopathy. These findings are consistent with prior reports implicating ferroptosis in cardiac injury, including myocardial ischemia-reperfusion injury and doxorubicin-induced cardiomyopathy, and suggest that a similar ferroptotic mechanism may also operate in the uremic setting [13,30,31].

A central finding of our study is that IS activates AhR signaling to induce ACSL4 expression. IS is a well-established endogenous agonist of AhR, and AhR activation has been implicated in cardiovascular inflammation and oxidative stress in the uremic milieu [32,33]. However, a direct AhR-dependent pro-ferroptotic transcriptional program in cardiomyocytes, particularly in the uremic heart, has not been clearly established [34,35]. We found that IS promoted AhR nuclear translocation in H9c2 cells, and that the AhR antagonist CH-223191 effectively blocked both AhR nuclear accumulation and ACSL4 upregulation at the mRNA and protein levels. Notably, AhR mRNA levels remained comparable across groups, suggesting that IS enhances AhR transcriptional activity through ligand-dependent activation rather than by increasing AhR abundance. These pharmacological data are consistent with AhR signaling contributing to IS-induced ACSL4 upregulation in cardiomyocytes. However, the formal requirement of AhR for this effect remains to be validated by genetic loss-of-function approaches.

An important caveat of our mechanistic conclusion warrants explicit discussion. Although pharmacological inhibition of AhR by CH-223191 effectively blocked IS-induced ACSL4 upregulation, and bioinformatic analysis identified multiple canonical XRE core motifs in the proximal ACSL4 promoter, these findings together constitute indirect rather than direct evidence for AhR-mediated transcriptional regulation of ACSL4. Direct physical binding of AhR to specific XRE elements within the ACSL4 promoter, as well as the functional necessity of these elements for IS-induced ACSL4 transactivation, were not experimentally validated in the present study by chromatin immunoprecipitation (ChIP)-qPCR, promoter-luciferase reporter assays, or site-directed mutagenesis of the predicted XRE motifs. We therefore interpret our findings as supporting an AhR-dependent regulatory relationship between IS exposure and ACSL4 induction, while acknowledging that formal demonstration of direct AhR-ACSL4 promoter binding remains an important objective for future studies. Notably, convergent evidence from AhR pharmacological antagonism, IS-induced AhR nuclear translocation, ACSL4 mRNA and protein induction, and *in silico* promoter scanning collectively renders this regulatory relationship plausible and biologically coherent, even in the absence of direct binding evidence. In addition, our conclusion regarding the involvement of AhR in IS-induced ACSL4 upregulation and cardiomyocyte ferroptosis relies primarily on pharmacological inhibition with CH-223191. Although CH-223191 is a widely used and well-characterized AhR antagonist (IC50 $\approx$ 30 nM) that effectively blocked both IS-induced AhR nuclear translocation and ACSL4 induction in our system, providing orthogonal pharmacological evidence for an AhR-dependent process, off-target activities of CH-223191 unrelated to AhR have been reported and cannot be entirely excluded. Genetic loss-of-function approaches, such as siRNA-mediated AhR knockdown or AhR knockout, combined with AhR rescue experiments, would be required to formally establish AhR as a non-

redundant upstream regulator in this pathway. We have therefore framed our conclusions accordingly throughout the manuscript and consider these genetic validation experiments, together with the ChIP-qPCR and reporter assays discussed above, as essential next steps to consolidate the proposed AhR/ACSL4/ferroptosis axis.

Functionally, our *in vitro* experiments support a ferroptotic mechanism in which the rescue of IS-induced injury by the selective ferroptosis inhibitor ferrostatin-1, which does not affect apoptosis or necroptosis, provides pharmacological specificity. Both genetic silencing of ACSL4 and ferrostatin-1 significantly attenuated IS-induced lipid peroxidation and rescued cell viability. The observation that ferrostatin-1 suppresses lipid peroxidation and cell death without reducing ACSL4 protein levels is mechanistically consistent with its known function as a lipophilic radical-trapping antioxidant that inhibits phospholipid peroxidation downstream of ACSL4-dependent PUFA-phospholipid remodeling [29]. Conversely, ACSL4 knockdown reduced lipid peroxidation, consistent with the established role of ACSL4 in promoting the incorporation of polyunsaturated fatty acids (PUFAs) into membrane phospholipids and thereby increasing their susceptibility to oxidation. ACSL4 knockdown was also accompanied by partial preservation of GPX4 protein levels. This finding should be interpreted with caution, as ACSL4 and GPX4 represent two distinct and largely independent arms of the ferroptotic process. ACSL4 governs the availability of oxidizable PUFA-phospholipid substrate, whereas GPX4 detoxifies lipid hydroperoxides, and our data do not indicate a direct regulatory relationship between ACSL4 and GPX4. Rather, the partial preservation of GPX4 following ACSL4 knockdown is most plausibly a secondary consequence of reduced lipid peroxidation and attenuated overall ferroptotic stress, as GPX4 downregulation may itself occur downstream of, or in parallel with, ongoing lipid peroxidation. Delineating whether and how ACSL4 manipulation influences GPX4 abundance would require additional dedicated mechanistic studies. These results align with the established role of ACSL4 as a key determinant of ferroptosis sensitivity and suggest that ACSL4-dependent ferroptotic remodeling is also relevant in CKD-associated (uremic) cardiomyopathy [5,36].

To extend these *in vitro* findings to an *in vivo* setting while isolating IS as a single, defined variable, we employed a direct IS injection model in non-CKD mice combined with AAV9-mediated cardiac-targeted ACSL4 knockdown. A critical aspect of our experimental design was the demonstration that AAV9-shACSL4 did not alter circulating IS concentrations, thereby confirming that the observed attenuation of cardiac structural remodeling and myocardial ferroptosis reflects local cardiac ACSL4 suppression rather than changes in systemic toxin burden. Cardiac ACSL4 knockdown significantly attenuated IS-induced increases in BNP, cardiac hypertrophy indices, myocardial fibrosis, and cardiomyocyte cross-sectional area, and concurrently reduced ferroptosis markers, including 4-HNE staining, iron deposition, MDA, and the disrupted GSH/GSSG ratio. These results provide strong evidence that ACSL4-dependent ferroptosis is a functionally important mediator of IS-induced cardiac injury *in vivo*. It should be noted, however, that the cardioprotection observed here was defined at the level of structural remodeling (hypertrophy and fibrosis), the wall-stress biomarker BNP, and molecular and biochemical ferroptosis indices, whereas systolic and diastolic cardiac function were not directly evaluated by echocardiography. Accordingly, our findings demonstrate that cardiac ACSL4 knockdown attenuates IS-induced structural and ferroptotic cardiac injury, although direct evidence of functional cardiac protection, as assessed by echocardiographic parameters including ejection fraction, fractional shortening, and diastolic indices, remains to be established. Given that IS is one of the major protein-bound uremic toxins that accumulate in CKD, these findings suggest that cardiac ACSL4 may represent a candidate therapeutic target warranting further evaluation in the context of uremic cardiomyopathy, although confirmation in models that more fully recapitulate the uremic milieu will be required.

From a translational perspective, our findings have several implications. They highlight ferroptosis as a tractable cell death pathway in uremic cardiomyopathy, complementing established roles of apoptosis, necroptosis, and autophagy in CKD-associated cardiac injury. The identification of AhR as an upstream regulator of ACSL4-mediated ferroptosis suggests that strategies aimed at modulating AhR activity or reducing systemic IS levels, such as oral adsorbents like AST-120, dietary tryptophan restriction, or gut microbiome modulation, may confer cardioprotective benefits through ferroptosis suppression. Importantly, such IS-lowering interventions would also serve as orthogonal *in vivo* loss-of-function experiments to directly test the causal contribution of IS to myocardial ferroptosis in the CKD setting, complementing the IS gain-of-function evidence provided by the direct IS injection model in the present study. Future preclinical studies combining IS-lowering interventions (e.g., AST-120 supplementation or dietary tryptophan restriction) with CKD induction in the 5/6 Nx model would therefore have dual translational and mechanistic value, and represent an important next step toward establishing IS as a causal contributor of uremic cardiomyopathy. Also, ACSL4 itself may serve as both a biomarker for ferroptotic vulnerability and a therapeutic target in the uremic heart. Future preclinical studies evaluating ACSL4 inhibitors or ferroptosis-targeting agents in CKD models with long-term follow-up would be informative.

Several points regarding the clinical translatability of the *in vitro* IS exposure conditions warrant discussion. The IS concentration used in this study (0.5 mM, 500 μM) is ap-

proximately 2-fold higher than the highest reported serum total IS concentrations in patients with end-stage renal disease (ESRD; typically ~200–250 μM, occasionally reaching ~320 μM), and substantially higher than the free (non-protein-bound) IS fraction observed in CKD patients (typically ~10–30 μM in ESRD), given that IS is ~90% albumin-bound under physiological conditions. We selected 0.5 mM based on three considerations. This concentration and exposure duration (24 h) are widely adopted across the published *in vitro* literature on IS-induced cardiomyocyte injury, with multiple seminal studies demonstrating robust hypertrophic, oxidative, and pro-fibrotic responses in H9c2 cells at 0.25–1 mM IS [9,28]. Use of a comparable concentration enables direct comparison of our findings with prior work and reinforces the convergence of mechanistic conclusions across studies. In addition, standard cell culture media (DMEM with 10% FBS) contain only a fraction of the albumin found in serum (~0.4 g/dL vs. ~3.5–5 g/dL), substantially reducing the protein-binding buffer for IS and altering the relationship between total and free IS *in vitro* relative to plasma. Consequently, the effective free IS exposure in our cultured cells is expected to be a higher proportion of the nominal added concentration than would be the case *in vivo*, partially offsetting the apparent excess of total IS. Further, acute *in vitro* exposure (24 h) is intended to recapitulate, in a tractable experimental window, the cumulative cellular impact of chronic IS exposure that accrues over months to years in CKD patients. Higher concentrations are therefore commonly used to overcome the kinetic mismatch between *in vitro* and *in vivo* exposure timescales. Nonetheless, we acknowledge that 0.5 mM IS represents a supraphysiological condition relative to absolute patient serum levels and that systematic dose-response and time-course experiments, including evaluation of IS in the lower end of the clinically relevant range (e.g., 50–250 μM total IS, or 10–50 μM in albumin-supplemented media to approximate the free IS fraction), would further strengthen the clinical translatability of the proposed AhR/ACSL4/ferroptosis mechanism. Such experiments represent an important next step in characterizing the concentration- and time-dependence of IS-induced cardiomyocyte ferroptosis.

Several limitations should be acknowledged. Regarding the proposed mechanism, the AhR-mediated transcriptional regulation of ACSL4 rests on pharmacological and *in silico* evidence rather than direct molecular proof. Direct AhR binding to XRE motifs within the ACSL4 promoter was not validated by ChIP-qPCR, promoter-luciferase reporter assays, or site-directed XRE mutagenesis. The requirement of AhR was also inferred primarily from the antagonist CH-223191, whose off-target activities cannot be completely excluded. Genetic AhR knockdown or knockout with rescue experiments, and direct *in vivo* AhR modulation, will be needed to establish AhR as a non-redundant upstream regulator. In addition, the *in vivo* cardiac ACSL4 knockdown was performed in the IS injection model rather than the 5/6 Nx CKD model, demonstrating that cardiac ACSL4 knockdown is protective within true CKD, which would provide the most direct genetic evidence for the proposed axis. Regarding the models and exposure conditions, the direct IS injection model isolates a single uremic toxin and does not reproduce the multifactorial uremic milieu of CKD, including renal dysfunction, hypertension, anemia, phosphate/FGF23 dysregulation, and systemic inflammation, all of which may modify IS-driven myocardial ferroptosis. The loss-of-function complement, namely whether reducing systemic IS levels (e.g., with AST-120, dietary tryptophan restriction, or microbiome modulation) attenuates myocardial ferroptosis in the CKD model, was not evaluated. The *in vitro* experiments used a single IS concentration (0.5 mM, 24 h) without dose-response or time-course characterization, relied on the H9c2 cardiomyoblast line rather than primary or human cardiomyocytes, and did not include si-ACSL4-alone or ferrostatin-1-alone basal controls. Whether other uremic toxins contribute to AhR-dependent ferroptosis, and whether the AhR/ACSL4 axis interacts with other regulated cell death pathways, also remains open. Regarding phenotyping and methodology, cardiac function was not directly assessed; echocardiographic evaluation of systolic and diastolic parameters would be required to substantiate functional cardiac protection. The identification of ferroptosis relied on convergent but individually non-specific markers, and would be strengthened by transmission electron microscopy, *in situ* lipid ROS imaging, iron chelation, and *in vivo* rescue with ferroptosis inhibitors. Several *in vivo* assays were performed on whole-heart tissue or sections without cardiomyocyte-specific co-staining. Although the cardiomyocyte-restricted cTnT promoter and H9c2 data support cardiomyocyte involvement, co-localization of ferroptosis markers with cTnT or α-actinin and direct measurement of ACSL4 in liver, kidney, skeletal muscle, and vascular tissue would further confirm the cell-type and organ specificity of the AAV9-cTnT-shACSL4 strategy. Serum IS was quantified by ELISA, which is adequate for relative between-group comparison but less definitive than LC-MS/MS for absolute quantification. Finally, only male mice were studied, and the AhR/ACSL4/ferroptosis axis cannot be assumed to operate identically in females; inclusion of both sexes is an important consideration for future work.

Conclusion

In summary, the present study demonstrates that the uremic toxin IS induces cardiomyocyte ferroptosis in association with activation of AhR signaling and upregulation of ACSL4. Cardiac-targeted ACSL4 knockdown attenuates IS-induced cardiac structural remodeling and myocardial ferroptosis *in vivo*. Although this knockdown was performed in the IS injection model rather

than in a CKD model, convergent evidence supports the AhR/ACSL4/ferroptosis axis as a candidate pathogenic mechanism in uremic cardiomyopathy, which warrants further validation in CKD models.

Availability of Data and Materials

The data that support the findings of this study are available from the corresponding authors upon reasonable request.

Author Contributions

DHZ, ZBL and JFL designed the research study. DHZ, ZBL and XHY performed the research. JFL, JFY and WWF analyzed the data. DHZ, JFY and JFL drafted the article. All authors contributed to important editorial changes in the manuscript. All authors gave final approval of the version to be published. All authors have participated sufficiently in the work to take public responsibility for appropriate portions of the content and agreed to be accountable for all aspects of the work in ensuring that questions related to its accuracy or integrity.

Ethics Approval and Consent to Participate

All animal procedures were approved by the Institutional Animal Care and Use Committee of Guangzhou University of Chinese Medicine (Approval No. 20250104008), and conformed to the National Institutes of Health Guide for the Care and Use of Laboratory Animals.

Acknowledgment

Not applicable.

Funding

This research received no external funding.

Conflict of Interest

The authors declare no conflict of interest.

Supplementary Material

Supplementary material associated with this article can be found, in the online version, at https://doi.org/10.24976/Discov.Med.202638209.156.

References

[1] GBD Chronic Kidney Disease Collaboration. Global, regional, and national burden of chronic kidney disease, 1990–2017: a systematic analysis for the Global Burden of Disease Study 2017. Lancet (London, England). 2020; 395: 709–733. https://doi.org/10.1016/S0140-6736(20)30045-3.

[2] Bello AK, Okpechi IG, Osman MA, Cho Y, Htay H, Jha V, *et al*. Epidemiology of haemodialysis outcomes. Nature Reviews. Nephrology. 2022; 18: 378–395. https://doi.org/10.1038/s41581-022-00542-7.

[3] Hayer MK, Radhakrishnan A, Price AM, Liu B, Baig S, Weston CJ, *et al*. Defining Myocardial Abnormalities Across the Stages of Chronic Kidney Disease: A Cardiac Magnetic Resonance Imaging Study. JACC. Cardiovascular Imaging. 2020; 13: 2357–2367. https://doi.org/10.1016/j.jcmg.2020.04.021.

[4] Porras CP, Dal Canto E, van Ommen AML, Handoko ML, Haitjema S, de Groot MCH, *et al*. Left Ventricular Diastolic Dysfunction across Levels of Kidney Function: A Cross-Sectional Study Based on Routine Clinical Practice Data. Journal of Clinical Medicine. 2024; 13: 5313. https://doi.org/10.3390/jcm13175313.

[5] Edwards NC, Pavlovic D, Ferro CJ, Townend JN. Chronic kidney disease-associated cardiomyopathy: clinical features, pathophysiology and treatment. Nature Reviews. Cardiology. 2026; 23: 392–406. https://doi.org/10.1038/s41569-025-01234-y.

[6] Yamaguchi K, Yisireyili M, Goto S, Cheng XW, Nakayama T, Matsushita T, *et al*. Indoxyl Sulfate Activates NLRP3 Inflammasome to Induce Cardiac Contractile Dysfunction Accompanied by Myocardial Fibrosis and Hypertrophy. Cardiovascular Toxicology. 2022; 22: 365–377. https://doi.org/10.1007/s12012-021-09718-2.

[7] Berg AH, Kumar S, Karumanchi SA. Indoxyl sulfate in uremia: an old idea with updated concepts. The Journal of Clinical Investigation. 2022; 132: e155860. https://doi.org/10.1172/JCI155860.

[8] Li Q, Zhang S, Wu QJ, Xiao J, Wang ZH, Mu XW, *et al*. Serum total indoxyl sulfate levels and all-cause and cardiovascular mortality in maintenance hemodialysis patients: a prospective cohort study. BMC Nephrology. 2022; 23: 231. https://doi.org/10.1186/s12882-022-02862-z.

[9] Yang K, Xu X, Nie L, Xiao T, Guan X, He T, *et al*. Indoxyl sulfate induces oxidative stress and hypertrophy in cardiomyocytes by inhibiting the AMPK/UCP2 signaling pathway. Toxicology Letters. 2015; 234: 110–119. https://doi.org/10.1016/j.toxlet.2015.01.021.

[10] Dixon SJ, Olzmann JA. The cell biology of ferroptosis. Nature Reviews. Molecular Cell Biology. 2024; 25: 424–442. https://doi.org/10.1038/s41580-024-00703-5.

[11] Xie Y, Hou W, Song X, Yu Y, Huang J, Sun X, *et al*. Ferroptosis: process and function. Cell Death and Differentiation. 2016; 23: 369–379. https://doi.org/10.1038/cdd.2015.158.

[12] Wang K, Chen XZ, Wang YH, Cheng XL, Zhao Y, Zhou LY, *et al*. Emerging roles of ferroptosis in cardiovascular diseases. Cell Death Discovery. 2022; 8: 394. https://doi.org/10.1038/s41420-022-01183-2.

[13] Cai W, Liu L, Shi X, Liu Y, Wang J, Fang X, *et al*. Alox15/15-HpETE Aggravates Myocardial Ischemia-Reperfusion Injury by Promoting Cardiomyocyte Ferroptosis. Circulation. 2023; 147: 1444–1460. https://doi.org/10.1161/CIRCULATIONAHA.122.060257.

[14] Wang X, Chen X, Zhou W, Men H, Bao T, Sun Y, *et al*. Ferroptosis is essential for diabetic cardiomyopathy and is prevented by sulforaphane *via* AMPK/NRF2 pathways. Acta Pharmaceutica Sinica. B. 2022; 12: 708–722. https://doi.org/10.1016/j.apsb.2021.10.005.

[15] Wang J, Wang Y, Liu Y, Cai X, Huang X, Fu W, *et al*. Ferroptosis, a new target for treatment of renal injury and fibrosis in a 5/6 nephrectomy-induced CKD rat model. Cell Death Discovery. 2022; 8: 127. https://doi.org/10.1038/s41420-022-00931-8.

[16] Li S, Han Q, Liu C, Wang Y, Liu F, Pan S, *et al*. Role of ferroptosis in chronic kidney disease. Cell Communication and Signaling: CCS. 2024; 22: 113. https://doi.org/10.1186/s12964-023-01422-8.

[17] Zhang HL, Hu BX, Li ZL, Du T, Shan JL, Ye ZP, *et al*. PKCβII phosphorylates ACSL4 to amplify lipid peroxidation to induce ferroptosis. Nature Cell Biology. 2022; 24: 88–98. https://doi.org/10.1038/s41556-021-00818-3.

[18] Kagan VE, Mao G, Qu F, Angeli JPF, Doll S, Croix CS, *et al*. Oxidized arachidonic and adrenic PEs navigate cells to ferroptosis. Nature Chemical Biology. 2017; 13: 81–90. https://doi.org/10.1038/nchembio.2238.

[19] Huang Q, Ru Y, Luo Y, Luo X, Liu D, Ma Y, *et al*. Identification of a targeted ACSL4 inhibitor to treat ferroptosis-related diseases. Science Advances. 2024; 10: eadk1200. https://doi.org/10.1126/sciadv.adk1200.

[20] Linghu M, Luo X, Zhou X, Liu D, Huang Q, Ru Y, *et al*. Covalent inhibition of ACSL4 alleviates ferroptosis-induced acute liver injury. Cell Chemical Biology. 2025; 32: 942–954.e5. https://doi.org/10.1016/j.chembiol.2025.06.004.

[21] Qiu M, Yan W, Liu M. YAP Facilitates NEDD4L-Mediated Ubiquitination and Degradation of ACSL4 to Alleviate Ferroptosis in Myocardial Ischemia-Reperfusion Injury. The Canadian Journal of Cardiology. 2023; 39: 1712–1727. https://doi.org/10.1016/j.cjca.2023.07.030.

[22] Hankinson O. The aryl hydrocarbon receptor complex. Annual Review of Pharmacology and Toxicology. 1995; 35: 307–340. https://doi.org/10.1146/annurev.pa.35.040195.001515.

[23] Nguyen C, Edgley AJ, Kelly DJ, Kompa AR. Aryl Hydrocarbon Receptor Inhibition Restores Indoxyl Sulfate-Mediated Endothelial Dysfunction in Rat Aortic Rings. Toxins. 2022; 14: 100. https://doi.org/10.3390/toxins14020100.

[24] Schroeder JC, Dinatale BC, Murray IA, Flaveny CA, Liu Q, Laurenzana EM, *et al*. The uremic toxin 3-indoxyl sulfate is a potent endogenous agonist for the human aryl hydrocarbon receptor. Biochemistry. 2010; 49: 393–400. https://doi.org/10.1021/bi901786x.

[25] Li Y, Feng D, Wang Z, Zhao Y, Sun R, Tian D, *et al*. Ischemia-induced ACSL4 activation contributes to ferroptosis-mediated tissue injury in intestinal ischemia/reperfusion. Cell Death and Differentiation. 2019; 26: 2284–2299. https://doi.org/10.1038/s41418-019-0299-4.

[26] Chen C, Xie C, Wu H, Wu L, Zhu J, Mao H, *et al*. Uraemic Cardiomyopathy in Different Mouse Models. Frontiers in Medicine. 2021; 8: 690517. https://doi.org/10.3389/fmed.2021.690517.

[27] Hamzaoui M, Djerada Z, Brunel V, Mulder P, Richard V, Bellien J, *et al*. 5/6 nephrectomy induces different renal, cardiac and vascular consequences in 129/Sv and C57BL/6JRj mice. Scientific Reports. 2020; 10: 1524. https://doi.org/10.1038/s41598-020-58393-w.

[28] Kishimoto H, Nakano T, Torisu K, Tokumoto M, Uchida Y, Yamada S, *et al*. Indoxyl sulfate induces left ventricular hypertrophy *via* the AhR-FGF23-FGFR4 signaling pathway. Frontiers in Cardiovascular Medicine. 2023; 10: 990422. https://doi.org/10.3389/fcvm.2023.990422.

[29] Miotto G, Rossetto M, Di Paolo ML, Orian L, Venerando R, Roveri A, *et al*. Insight into the mechanism of ferroptosis inhibition by ferrostatin-1. Redox Biology. 2020; 28: 101328. https://doi.org/10.1016/j.redox.2019.101328.

[30] Ta N, Qu C, Wu H, Zhang D, Sun T, Li Y, *et al*. Mitochondrial outer membrane protein FUNDC2 promotes ferroptosis and contributes to doxorubicin-induced cardiomyopathy. Proceedings of the National Academy of Sciences of the United States of America. 2022; 119: e2117396119. https://doi.org/10.1073/pnas.2117396119.

[31] Zhao Y, Linkermann A, Takahashi M, Li Q, Zhou X. Ferroptosis in cardiovascular disease: regulatory mechanisms and therapeutic implications. European Heart Journal. 2025; 46: 3247–3260. https://doi.org/10.1093/eurheartj/ehaf374.

[32] Nakagawa K, Itoya M, Takemoto N, Matsuura Y, Tawa M, Matsumura Y, *et al*. Indoxyl sulfate induces ROS production via the aryl hydrocarbon receptor-NADPH oxidase pathway and inactivates NO in vascular tissues. Life Sciences. 2021; 265: 118807. https://doi.org/10.1016/j.lfs.2020.118807.

[33] Lano G, Laforêt M, Von Kotze C, Perrin J, Addi T, Brunet P, *et al*. Aryl Hydrocarbon Receptor Activation and Tissue Factor Induction by Fluid Shear Stress and Indoxyl Sulfate in Endothelial Cells. International Journal of Molecular Sciences. 2020; 21: 2392. https://doi.org/10.3390/ijms21072392.

[34] Liao Z, Huang M, Zhang Y, Huang S, Lei W, Shui X. Potential role of AhR in ischemia-reperfusion injury and cancers: Focus on ferroptosis and lipid peroxidation signaling pathways (Review). International Journal of Molecular Medicine. 2025; 56: 156. https://doi.org/10.3892/ijmm.2025.5597.

[35] Zhang Y, Han X, Feng T, Li Z, Yu H, Chen Y, *et al*. Gut-microbiota-derived indole sulfate promotes heart failure in chronic kidney disease. Cell Host & Microbe. 2025; 33: 1715–1730.e5. https://doi.org/10.1016/j.chom.2025.08.014.

[36] Xiao D, Chang W, Ao X, Ye L, Wu W, Song L, *et al*. Parkin inhibits iron overload-induced cardiomyocyte ferroptosis by ubiquitinating ACSL4 and modulating PUFA-phospholipids metabolism. Acta Pharmaceutica Sinica. B. 2025; 15: 1589–1607. https://doi.org/10.1016/j.apsb.2024.12.027.